Light Scattering from Collagen Fiber Networks: Micro-Optical Properties of Normal and Neoplastic Stroma

Dizem Arifler,* Ina Pavlova,† Ann Gillenwater,‡ and Rebecca Richards-Kortum§

*Department of Physics, Eastern Mediterranean University, Famagusta, Cyprus; †Department of Biomedical Engineering, The University of Texas at Austin, Austin, Texas; ‡Department of Head and Neck Surgery, The University of Texas M. D. Anderson Cancer Center, Houston, Texas; and §Department of Bioengineering, Rice University, Houston, Texas

ABSTRACT Development of epithelial precancer and cancer leads to well-documented molecular and structural changes in the epithelium. Recently, it has been recognized that stromal biology is also altered significantly with preinvasive disease. We used the finite-difference time-domain method, a popular technique in computational electromagnetics, to model light scattering from heterogeneous collagen fiber networks and to analyze how neoplastic changes alter stromal scattering properties. Three-dimensional optical images from the stroma of fresh normal and neoplastic oral-cavity biopsies were acquired using fluorescence confocal microscopy. These optical sections were then processed to create realistic three-dimensional collagen networks as model input. Image analysis revealed that the volume fraction of collagen fibers in the stroma decreases with precancer and cancer progression, and fibers tend to be shorter and more disconnected in neoplastic stroma. The finite-difference time-domain modeling results showed that neoplastic fiber networks have smaller scattering cross sections compared to normal networks. Computed scattering-phase functions indicate that high-angle scattering probabilities tend to be higher for neoplastic networks. These results provide valuable insight into the micro-optical properties of normal and neoplastic stroma. Characterization of optical signals obtained from epithelial tissues can aid in development of optical spectroscopic and imaging techniques for noninvasive monitoring of early neoplastic changes.

INTRODUCTION

Over the last 50 years, there have been tremendous advances in our understanding of the molecular and cellular processes of cancer, and great progress in the treatment of a number of neoplastic disorders; however, there has been no change in the age-adjusted mortality due to cancer over this same period (1,2). Patients who present with early-stage disease have better chances for cure and less treatment-associated morbidity. When cancer patients present with tumors at advanced stages, treatment is more difficult, more expensive, and less successful compared to earlier interventions. Thus, early detection of neoplastic changes may be our best method to improve patient quality of life and reduce cancer mortality.

More than 85% of cancers arise in epithelial tissues and are preceded by a precancerous stage in which neoplastic cells are confined to the epithelium. In a number of organ sites, screening for precancerous changes followed by appropriate therapy has been shown to reduce both cancer mortality and cancer incidence (2). Epithelial precancers and cancers are associated with a variety of well-documented morphologic and architectural alterations, including increased nuclear size, increased nucleus/cytoplasm ratio, hyperchromasia, pleomorphism, and loss of normal epithelial architecture (3). Cytologic screening and histopathologic detection of preinvasive lesions currently rely largely on identification of these epithelial changes.

However, neoplasia is associated with alterations in both epithelial cells and the supporting stroma (4,5). Tumor progression involves complex interactions between neoplastic cells, extracellular matrix, and stromal cells (6,7), and carcinogenesis results, in part, from defective epithelial-stromal communication (8,9). Recently, it has been recognized that alterations in stromal biology may precede and stimulate neoplastic progression in preinvasive disease (8,10). Monitoring these stromal changes may provide additional targets to aid in screening and early detection of precancerous changes.

A number of optical spectroscopic and imaging techniques have recently been explored as tools to improve the in vivo, real-time detection of epithelial precancers and cancers (11–19). Development of optical technologies for biomedical applications necessitates a detailed understanding of the micro-optical properties of biological tissues. Structural and morphological changes in microscopic tissue constituents result in alteration of their light-scattering characteristics, giving rise to optical contrast that can be detected in vivo and be used to monitor changes associated with disease progression.

Numerous modeling studies have been carried out to analyze the scattering properties of biological cells or cell components. These studies involve analyses based on Mie theory or analytical approximations (20–26). Recently, the finite-difference time-domain (FDTD) method, which numerically solves Maxwell's equations, has provided a flexible computational framework to study light scattering from cells or cell components of arbitrary shape and complex internal

Submitted May 24, 2006, and accepted for publication January 17, 2007.

Address reprint requests to Rebecca Richards-Kortum, Rice University, Dept. of Bioengineering, 6100 Main St., Houston, TX 77005. Tel.: 713-348-3823; Fax: 713-348-5877; E-mail: rkortum@rice.edu.

0006-3495/07/05/3260/15 $2.00

doi: 10.1529/biophysj.106.089839

structure (27–31). For amelanotic epithelial tissues that have a low fraction of cellular organelles, cell nuclei are the main sources of scattering in the epithelium (20,32,33). The FDTD method has been used to investigate how the scattering properties of epithelial cell nuclei are affected by changes in nuclear morphology and chromatin texture that occur with neoplastic progression (34,35). FDTD modeling results can be used to better interpret tissue spectra obtained with scattering-based optical spectroscopic techniques that are emerging as potential tools for noninvasive detection of precancerous changes in epithelial tissues (13,16,17,19). Results from FDTD simulations also provide important insights into intrinsic optical contrast observed in images obtained using reflectance confocal microscopy (RCM), optical coherence tomography (OCT), and optical coherence microscopy (OCM), which are promising backscattering-based optical imaging technologies for detection of epithelial precancer and cancer (14,15,18).

Collagen fibers are the main scatterers in the stroma underlying the epithelium, but little is known about their scattering properties. Due to the high refractive index and fibrous nature of collagen fibers, scattering in the stroma is much higher than scattering in the epithelial layer of amelanotic tissues (36–39). Stromal scattering contributes significantly to spectroscopic reflectance signals acquired from epithelial tissues. Therefore, characterization of stromal scattering is necessary to better interpret spectral signatures and to develop more reliable computational models to describe light transport in epithelial tissues. Extensive efforts have recently been made to optimize design of fiberoptic probes or to develop techniques and algorithms to separate spectroscopic signatures from different tissue layers (21,22,40–45). These efforts are likely to benefit from a more comprehensive understanding of stromal scattering.

Further, neoplastic progression is associated with regulation of matrix-degrading proteases essential in invasion and metastasis (4,7). The resulting structural changes in the stromal collagen matrix and possible decomposition of collagen fibers (46–49) lead to changes in stromal scattering (37,38). Thus, there may be clinically relevant information in optical signals from the stroma. Analysis of the scattering characteristics of collagen fibers may be an important step toward depicting a more complete picture of changes in optical properties of neoplastic tissues. From an imaging perspective, the penetration depth achievable with RCM is usually limited to the epithelial layer, but modalities such as OCT and OCM are capable of probing the stromal layer. Two-dimensional, multispectral imaging systems are also sensitive to stromal optical properties. Any optical contrast resulting from differences in scattering properties of normal and neoplastic stroma can be used as an additional diagnostic measure for in vivo detection of preinvasive disease.

The number of studies analyzing the scattering properties of collagen fibers is very limited. This is partly due to the lack of available information about specific morphology, structure, and orientation of fibers constituting the collagen matrix. Freund et al. (50) studied the effects of fibril orientation on light scattering in the cornea by treating the fibrils as parallel finite-length cylinders. Since collagen fibrils in the corneal stroma have a highly regular spatial arrangement, assumption of aligned cylindrical scatterers is justified. Saidi et al. (51) modeled scattering by collagen fibers in neonatal skin using two-dimensional cylindrical Mie theory. In this study, the fibers were assumed to be infinitely long cylinders that ran parallel to the tissue surface. Organization of the collagen matrix and orientation of collagen fibers in the matrix can vary significantly for different tissue types. Stroma beneath the epithelia lining the internal surfaces of the body is characterized by collagen fibers that are randomly oriented and intricately interlaced (52,53). In these tissues, collagen fibers are not unidirectional and can have extremely irregular alignment. Thus, description of these fibers as simple cylindrical scatterers may be an oversimplification. Since the FDTD method does not put any limitations on the scattering structure to be simulated, it provides a flexible approach to study scattering from randomly oriented and interlaced collagen fibers. In such cases, however, it is extremely difficult to quantify the length, diameter, or orientation of fibers, and to create realistic three-dimensional models for light-scattering analysis.

Histological staining and electron microscopy have been widely used to observe and study the structural properties of collagen fibers (52–54), but fixation and dehydration associated with these techniques are likely to affect the organization and volume fraction of fibers in the stroma. A more suitable approach to study the complex nature of the fibrous networks created by collagen fibers has been proposed in a recent study by Wu et al. (55) that describes reconstruction of fibers in a collagen gel from optical sections acquired using a reflectance confocal microscope. An image-processing algorithm developed in conjunction with confocal imaging is used to create surface-rendered images of the collagen gel, enabling three-dimensional visualization. Collagen is a well-known source of autofluorescence and nonlinear emission (56,57). Therefore, other techniques that have the potential to enable three-dimensional structural visualization of collagen fibers involve fluorescence confocal microscopy, multiphoton microscopy, and second-harmonic-generation imaging, all of which can provide high contrast and optical-sectioning capabilities (57–59).

In this study, we used FDTD modeling to study light scattering from collagen fiber networks. To create realistic collagen network models, optical sections from the stroma of normal and neoplastic oral-cavity biopsy samples were acquired using fluorescence confocal microscopy. These optical sections provided realistic input for construction of three-dimensional collagen networks. FDTD modeling was then used to analyze the intensity and angular distribution of light scattered from the constructed fiber networks, and to

establish trends for neoplastic changes in stromal scattering properties.

METHODS

Finite-difference time-domain modeling

Implementation of the FDTD algorithm used in this study has been previously described (35). Briefly, a scattering object is constructed in a three-dimensional grid by specifying the dielectric properties of each grid cell belonging to the object. The Yee algorithm (60,61) is then used to compute the scattered electric- and magnetic-field components around the scattering object. This algorithm takes Maxwell's curl equations and discretizes them in space and time, resulting in a set of six explicit finite-difference equations, one for each electric- or magnetic-field component. The finite-difference equations are time-marched until the field values converge to a steady state. To simulate propagation in an unbounded medium, special boundary conditions must be applied to prevent artificial reflections at the edges of the FDTD computational grid. The perfectly-matched-layer boundary condition (60,61) creates a fictitious absorbing layer around the computational domain. Plane waves of arbitrary incidence, polarization, and frequency are matched at the boundary; thus, artificial reflections are suppressed. The finite-difference equations produce the time-domain near-field scattered electric- and magnetic-field components. To compute the far-field values, the time-domain tangential-field components on a surface S enclosing the scattering object are first converted to frequency-domain values using discrete Fourier transform. The next step is to calculate the electric and magnetic far-field components using Huygen's equivalence principle. Here, equivalent electric and magnetic surface-current densities are defined on S, and the far-field components are calculated by taking the spatial Fourier transforms of these current densities. The scattering patterns, normalized phase functions, and scattering cross-section values can then be computed using the far-field values (62).

Biopsy collection and confocal imaging of fresh tissue slices

This research was approved by the Institutional Review Boards at The University of Texas M. D. Anderson Cancer Center, The University of Texas at Austin, and Rice University. Clinically normal and abnormal oral-cavity biopsy pairs were obtained, with informed consent, from patients at The University of Texas M. D. Anderson Cancer Center. Biopsies remained in chilled tissue-culture medium until they were sectioned into 200-μm-thick transverse tissue slices with a Krumdieck tissue slicer (MD 1000-A1, Alabama Research and Development, Munford, AL). Each tissue slice was imaged with a confocal laser-scanning fluorescence microscope (SP2 AOBS, Leica Microsystems, Wetzlar, Germany) equipped with a 40×, 1.25 NA oil-immersion objective. Two wavelengths, 351 nm and 364 nm, were used to excite the tissue, with detection set from 380 nm to 550 nm. In this excitation wavelength range, stromal fluorescence is mainly attributed to collagen (56,63), enabling visualization of collagen fibers. Excitation of tissue through two different laser lines at the same time resulted in an improvement in the detected optical signal. Optical stacks were obtained from the tissue slices with an imaging field of view of 375 μm × 375 μm. The theoretical lateral and axial resolutions of the fluorescence confocal microscope were ~0.115 μm and 0.480 μm, respectively. In our imaging studies, the actual lateral resolution was limited by the lateral pixel size, which was set to 0.732 μm. The actual axial resolution was limited by the axial step size used to optically section the tissue samples, which was 1 μm. Each optical stack included 8–10 optical sections, corresponding to a total sampled depth of 8–10 μm. Since the diameter of the collagen fibers is expected to be on the order of several micrometers (52,53), such a resolution level is considered to be sufficient for image analysis.

Image processing for segmentation of collagen fibers and construction of collagen fiber networks for FDTD modeling

We implemented an image-processing algorithm in Matlab (The MathWorks, Natick, MA) to segment collagen fibers from a series of optical sections and to construct a three-dimensional collagen fiber network for direct input into the FDTD computational grid. The first step was to determine a region of interest in the stromal part of a confocal image. The selected region of interest corresponded to an area of 8 μm × 8 μm. Eight consecutive optical sections corresponding to the same lateral position were used to create a volume of interest with a size of 8 μm × 8 μm × 8 μm. Although the lateral position of each region of interest was randomly selected for each tissue slice, image analysis was restricted to locations within the first 200 μm below the basement membrane. The second step of the algorithm involved interpolation of the selected optical sections to represent the volume of interest with a finer grid size. FDTD modeling requires that the grid spacing for the computational domain be less than a given upper limit (60). Therefore, resampling the original volume of interest was necessary to satisfy this threshold and ensure the stability of the computations. Interpolation was first carried out in the lateral direction, and then in the axial direction. In both cases, cubic splines were used to interpolate the original pixel-intensity values. Next, each interpolated optical section was processed to segment out the collagen fibers. Segmentation was performed using a clustering algorithm. Fuzzy c-means clustering (64) was used to reduce the number of gray levels to two and to create a binary representation of the three-dimensional grid. In this binary representation, a voxel value of 0 indicates the outside medium surrounding the collagen fibers, and a voxel value of 1 indicates collagen. Implementing a clustering algorithm provided a simple, efficient means of segmenting collagen fibers in the three-dimensional grid and eliminated the necessity of resorting to threshold-based processing, which would require manual intervention.

The algorithm was applied to confocal image stacks obtained from three pairs of clinically normal and abnormal tongue, gingiva, or palate biopsies. Four networks were constructed from each biopsy by sampling different areas on the confocal images. Therefore, a total of 24 (12 normal and 12 abnormal) collagen fiber networks were available for FDTD simulations.

Characterization of collagen fiber networks

Volume fraction of collagen fibers

Volume fraction is defined as the fraction of the computational grid occupied by collagen fibers. This parameter is easy to compute, since each collagen fiber network can be described by a binary intensity function $I(x,y,z)$, which represents the occupation state of each voxel or grid cell in the computational domain at the coordinates (x,y,z).

Spatial organization of collagen fibers

In addition to the fraction of the computational grid occupied by collagen fibers, a metric is required to describe the texture of the collagen networks. Since stromal collagen fibers are characterized by random spatial orientation, a suitable approach to characterize three-dimensional texture is to use statistical features. Haralick features are widely used in the field of biomedical imaging to characterize natural textures and are computed based on co-occurrence matrices (65,66). These matrices describe the frequency of occurrence of pixel pairs with specified intensity levels. A co-occurrence matrix, $C_d(i,j)$, is a matrix where the (i,j)th element represents the frequency of occurrence of two neighboring pixels in direction d with gray levels i and j. For binary images, where i and j can only assume the values 0 and 1, the co-occurrence matrix will have four entries. Since collagen fiber networks are described by volumetric grid data, we can compute co-occurrence matrices separately for the three dimensions. If $I(x,y,z)$ represents the grid data

where a voxel value of 0 indicates outside medium, and a voxel value of 1 indicates collagen, the co-occurrence matrices for the x, y, and z directions are defined by

$$\begin{aligned} C_x(i,j) &= \text{number of voxels with } I(x,y,z) = i \\ &\quad \text{and} \quad I(x+1,y,z) = j, \\ C_y(i,j) &= \text{number of voxels with } I(x,y,z) = i \\ &\quad \text{and} \quad I(x,y+1,z) = j, \\ C_z(i,j) &= \text{number of voxels with } I(x,y,z) = i \\ &\quad \text{and} \quad I(x,y,z+1) = j, \end{aligned} \tag{1}$$

with $i, j \in \{0, 1\}$.

The matrices in Eq. 1 are generally normalized to express the matrix entries as probability measures. Normalized co-occurrence matrices are given by

$$\hat{C}_{x,y,z}(i,j) = \frac{C_{x,y,z}(i,j)}{\sum_i \sum_j C_{x,y,z}(i,j)}. \tag{2}$$

It is possible to define many different texture features using the normalized co-occurrence matrices. Two features that can be computed to characterize the collagen networks created are generally referred to as contrast and correlation. These parameters are defined as (65,66)

$$contrast_{x,y,z} = \sum_i \sum_j (i-j)^2 \times \hat{C}_{x,y,z}(i,j), \tag{3}$$

and

$$correlation_{x,y,z} = \sum_i \sum_j (i-\bar{I})(j-\bar{I}) \times \hat{C}_{x,y,z}(i,j), \tag{4}$$

where $\bar{I}$ is the mean intensity and is equal to the volume fraction due to the binary representation of the three-dimensional structure in question. Since contrast depends on the difference between i and j, this parameter is expected to assume large values when the three-dimensional structure has frequent intensity transitions from 0 to 1, or from 1 to 0. A large value for correlation indicates that the three-dimensional structure has large connected subcomponents.

Contrast and correlation values for the x, y, and z dimensions were calculated separately for each of the 24 collagen fiber networks created. These values are expected to provide some insight into the three-dimensional organization of the collagen fibers.

FDTD simulation parameters

The FDTD simulations for the collagen fiber networks created were performed at a vacuum wavelength of $\lambda = 1064$ nm, for a plane wave traveling in the z direction. This wavelength was chosen so that the results would be applicable to imaging techniques such as RCM, OCT, and OCM. The refractive index of the outside medium surrounding the collagen fibers was set to 1.35 (67–69). Grid cells corresponding to collagen fibers were assigned refractive indices that were randomly selected from the range 1.40–1.45 (68–71). The FDTD grid spacing used was 1/20 of the wavelength in the outside medium. This grid spacing is commonly employed in FDTD modeling, and was preset during the interpolation step of the algorithm used to create the collagen fiber networks. The size of each network was 8 μm $\times$ 8 μm $\times$ 8 μm, corresponding to $\sim$210 $\times$ 210 $\times$ 210 grid cells. The computational domain was extended to enable implementation of the perfectly-matched-layer boundary condition, but the memory required for each simulation did not exceed 2 Gb, allowing the computations to be carried out on a PC.

RESULTS

Confocal imaging of fresh tissue slices

Fig. 1 shows the stromal portion of the confocal images of tissue slices from a clinically normal and a clinically abnormal biopsy pair used in this study. The top parts of the images are roughly parallel to the basement membrane and hence to the tissue surface. Collagen fibers can be identified due to their bright autofluorescence. Note that the stroma of the normal tissue is characterized by dense collagen fibers (Fig. 1 *A*), whereas the stroma of the abnormal tissue is less dense and appears less structured (Fig. 1 *B*). The tissue sections imaged in this study were later submitted for histopathologic analysis. The abnormal sections were all classified as moderately or well differentiated invasive squamous cell carcinoma.

Constructed collagen fiber networks for FDTD modeling

Fig. 2 provides a step-by-step illustration of the image processing algorithm used to construct three-dimensional collagen fiber networks by showing the results for a particular image set after each intermediate step. In the figure, the x and z coordinates define the lateral image plane, and the y coordinate defines the axial direction. The three optical sections shown in Fig. 2 *A* are from different depths within the imaged tissue sample and correspond to the original confocal images on the top, in the middle, and at the bottom of the image stack. Fig. 2 *B* shows the interpolated image sections corresponding to the selected region of interest, whereas Fig. 2 *C* shows the same image sections after segmentation of collagen fibers. To give a better insight into the three-dimensional organization of the fibers, Fig. 2 *D* presents an isosurface-rendered representation of the collagen network created from the image stack. The figure demonstrates the random and irregular alignment of collagen fibers in the stroma, which is especially evident in the three-dimensional representation of the network. It is hard to quantify the organizational tendencies of the collagen fibers,

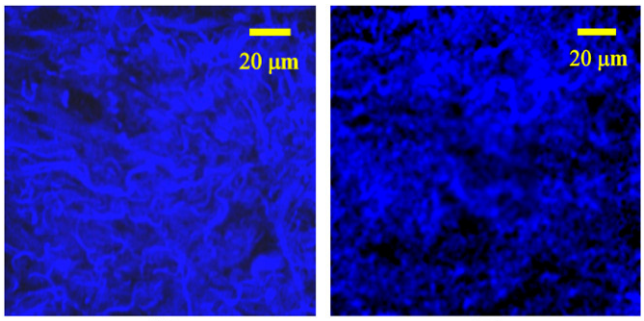

FIGURE 1 Stromal portion of the confocal images of tissue slices from (*A*) clinically normal, and (*B*) clinically abnormal biopsy pair. Collagen fibers are visible due to autofluorescence.

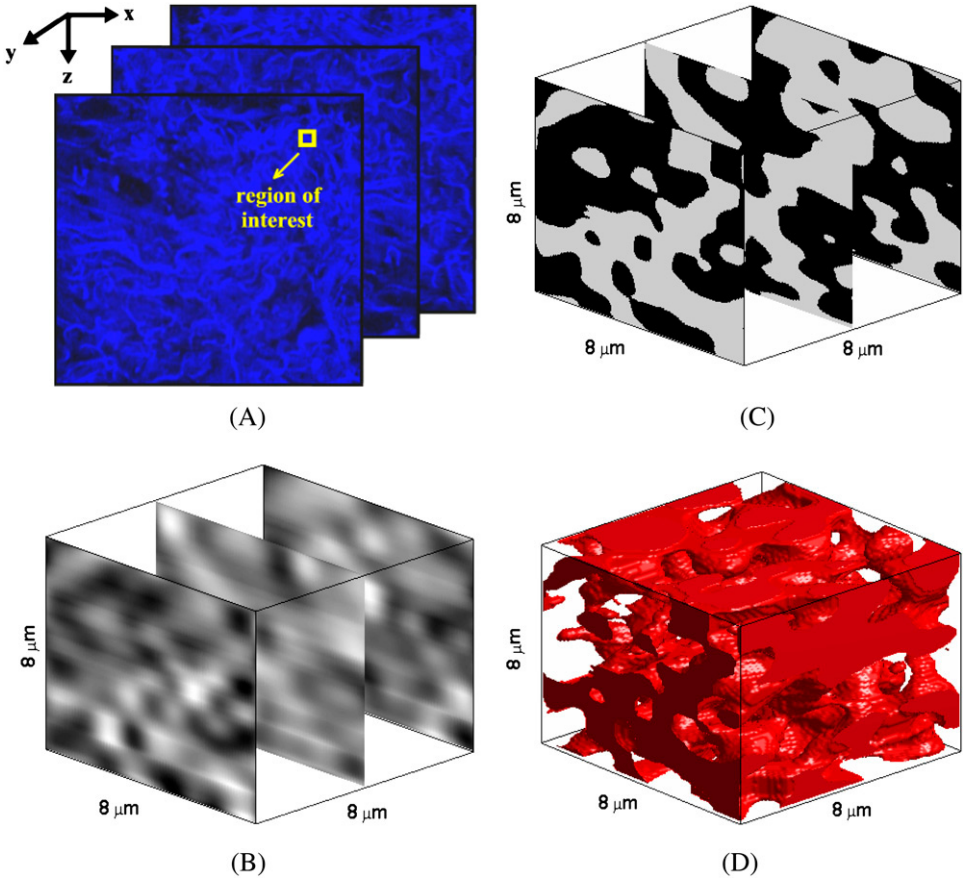

FIGURE 2 Construction of a three-dimensional collagen fiber network from a series of optical sections. (*A*) Selection of a region of interest in the original confocal image set, followed by (*B*) interpolation using cubic splines, and (*C*) segmentation of collagen fibers through fuzzy c-means clustering. (*D*) Isosurface-rendered representation of the collagen fiber network.

validating the necessity to resort to statistical features to distinguish structural differences.

Table 1 provides statistics about the structural parameters computed to characterize the collagen networks constructed. The table lists the 95% Student's *t* confidence intervals based on values obtained for four networks corresponding to each biopsy, under the assumption that the data values come from a normal distribution. Contrast and correlation values given represent averages over the *x*, *y*, and *z* dimensions. No specific trend was observed when the three directions were considered separately, suggesting no directional preference for collagen fiber organization. The table demonstrates that the volume fraction of collagen fibers for the abnormal or neoplastic biopsies is lower compared to the volume fraction for the normal biopsies, and the difference is ~20–25% for the three cases shown. Since the confidence intervals do not overlap, the averages of the volume fractions for normal and neoplastic biopsies are different with 95% confidence. The confidence intervals for the volume fractions are wider for the neoplastic biopsies in the case of the first two patients, indicating greater variability. Despite no observable trend for the contrast values, the averages of the correlation values for the normal and neoplastic biopsies are different with 95% confidence. Collagen fiber networks constructed from the neoplastic biopsies have lower correlation values compared to the collagen networks constructed from the normal biopsies. Lower correlation values suggest increased disorder in the three-dimensional organization of the collagen fibers. As in the case of the volume fraction, the confidence intervals are wider for the neoplastic cases.

TABLE 1 95% Student's *t* confidence intervals for structural parameters obtained from three-dimensional image analysis

	Volume fraction	Contrast	Correlation
Patient 1			
Normal	0.48 ± 0.01	0.020 ± 0.001	0.239 ± 0.001
Neoplastic	0.40 ± 0.04	0.021 ± 0.002	0.227 ± 0.011
Patient 2			
Normal	0.49 ± 0.02	0.021 ± 0.002	0.239 ± 0.001
Neoplastic	0.39 ± 0.04	0.019 ± 0.002	0.227 ± 0.010
Patient 3			
Normal	0.54 ± 0.02	0.023 ± 0.002	0.239 ± 0.002
Neoplastic	0.39 ± 0.02	0.018 ± 0.004	0.230 ± 0.005

The three-dimensional structural parameters presented in Table 1 were based on confocal image stacks of tissue slices from only three patients. To investigate whether these parameters are representative of typical stroma, we performed image analysis on confocal images of 18 additional normal oral-cavity biopsies and 11 additional abnormal biopsies obtained from patients diagnosed with moderately or well differentiated invasive oral cancer. These images were acquired

for another study, and optical stacks were not available for three-dimensional analysis. Instead, the image processing algorithm was applied in two dimensions. In accordance with the three-dimensional analysis, four regions of interest were selected from each confocal image, resulting in a total of 116 (72 normal and 44 abnormal) 8 μm $\times$ 8 μm image segments. We have also performed two-dimensional image analysis on 24 image segments from confocal images obtained from six mildly dysplastic oral-cavity biopsies and 12 image segments from confocal images obtained from three moderately dysplastic oral-cavity biopsies. Table 2 shows the 95% Student's t confidence intervals for two-dimensional structural parameters corresponding to different diagnostic categories. The table demonstrates that the averages of the area fractions of collagen fibers for normal and neoplastic biopsies are different with 95% confidence. The contrast values are again comparable, whereas the averages of the correlation values are different with 95% confidence. The confidence intervals presented in Table 2 for mildly and moderately dysplastic biopsies suggest that the structural parameters of precancerous samples tend to fall between those of normal and cancerous samples, with the exception of contrast values, which are comparable across all diagnostic categories. The results obtained from two-dimensional image analysis and presented in Table 2 are very close to the three-dimensional parameters listed in Table 1. Note also that the additional biopsies used for two-dimensional analysis were from different oral-cavity sites, including the floor of the mouth, retromolar trigone, palate, gingiva, buccal mucosa, and the tongue, which normally have markedly different histologic properties. This indicates that the three-dimensional collagen fiber networks used for FDTD simulations are valid models characterizing typical stromal organization.

To elucidate any interdependence among volume fraction, contrast, and correlation, Fig. 3, *A–C*, shows scatter plots of these parameters calculated for each of the three-dimensional collagen networks created. Scatter plots of contrast versus volume fraction, correlation versus volume fraction, and correlation versus contrast are shown in Fig. 3, *A–C*, respectively. Fig. 3, *D–F*, presents scatter plots of area fraction, contrast, and correlation values obtained from two-dimensional image analysis. The averages over four image segments are plotted, resulting in one data point for each biopsy analyzed. The trends observed for two-dimensional and three-dimensional image analysis are similar. The parameters that provide the best separation between normal and neoplastic cases are the volume or area fraction and the correlation, as also evidenced in Tables 1 and 2. The trends shown in Fig. 3, *B* and *E*, indicate that these two parameters are not independent, and correlation increases with increasing volume or area fraction. The relative rate of increase in correlation is higher for small volume or area fractions.

TABLE 2 95% Student's *t* confidence intervals for structural parameters obtained from two-dimensional image analysis

Diagnostic category	Number of biopsies analyzed	Area fraction	Contrast	Correlation
Normal	18	0.53 ± 0.02	0.020 ± 0.002	0.238 ± 0.001
Mildly dysplastic	6	0.48 ± 0.02	0.019 ± 0.002	0.238 ± 0.002
Moderately dysplastic	3	0.45 ± 0.04	0.018 ± 0.004	0.237 ± 0.003
Neoplastic	11	0.43 ± 0.01	0.020 ± 0.002	0.234 ± 0.002

FDTD simulation results

Scattering patterns

Fig. 4 shows the FDTD scattering patterns averaged over four collagen fiber networks corresponding to each biopsy. The averaged scattering patterns for the networks corresponding to the first patient are shown in Fig. 4 *A*, those for the second patient in Fig. 4 *B*, and those for the third patient in Fig. 4 *C*. All scattering patterns were averaged over the azimuthal angle so that they were functions of the scattering angle only. The light-colored curves in Fig. 4 represent the results for the normal collagen fiber networks, and the darker curves represent the results for the neoplastic collagen fiber networks. The angular resolution for the scattering angle is 1°, and the scattering intensity is given in arbitrary units. The averaged scattering patterns of the collagen fiber networks created have similar shape; they are highly peaked in the forward direction, and the scattering intensity covers a dynamic range of about six orders of magnitude.

Fig. 5 combines the scattering patterns shown in Fig. 4 by averaging the intensity values corresponding to each diagnostic category. This figure characterizes the angle-dependent scattering properties of normal versus neoplastic collagen fiber networks. Fig. 5 *A* shows the scattering patterns over the angular range 0–180°. It is apparent that differences in the scattering patterns of normal and neoplastic collagen fiber networks are rather subtle. Fig. 5 *B* zooms in on the scattering patterns for 0–40° to enhance intensity differences for small scattering angles, and Fig. 5 *C* zooms in on the scattering patterns for 140–180° to show differences in high-angle scattering. It is evident in Fig. 5 *B* that the intensity of light scattered in the forward direction is higher for the normal networks. The intensity for small scattering angles decreases in the case of neoplastic networks. On the other hand, Fig. 5 *C* shows that the intensity of high-angle scattering (170–180°) tends to be higher for the neoplastic networks.

Scattering-phase functions

A scattering-phase function is obtained by normalizing the scattering pattern so that its integral over the solid angle equals 1. Fig. 6 shows the phase functions corresponding to the scattering patterns in Fig. 4, whereas Fig. 7 shows the phase functions averaged over each diagnostic category. As in the case of Fig. 5, the averaged phase functions for the

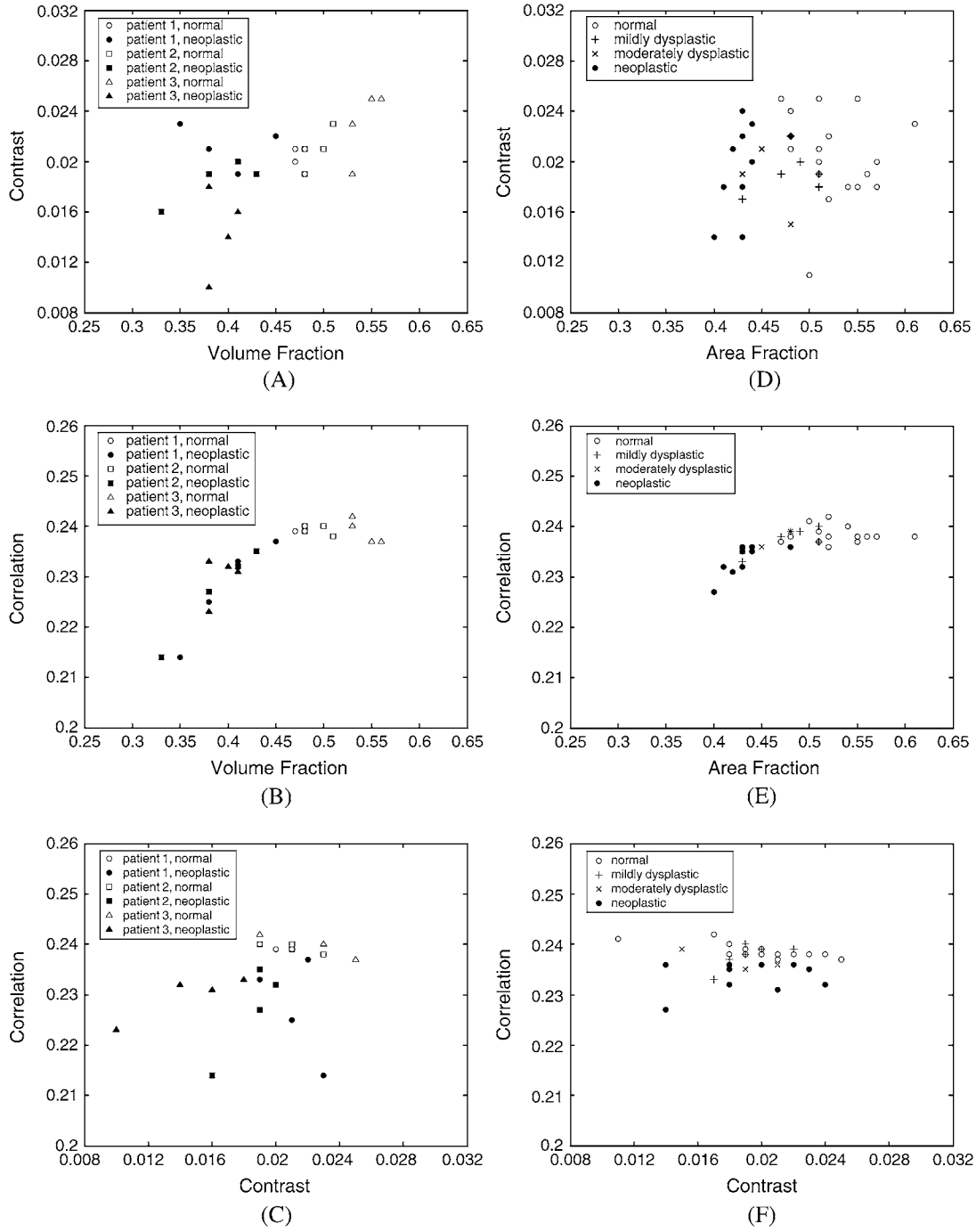

FIGURE 3 Scatter plots of structural parameters obtained from (*A–C*) three-dimensional, and (*D–F*) two-dimensional image analysis.

angular range 0–180° are shown in Fig. 7 *A*. Fig. 7, *B* and *C*, zooms in on regions of small-angle and high-angle scattering, respectively. As Fig. 7 *A* demonstrates, the overall shapes of the phase functions are very similar for small scattering angles. For angles $>\sim 20°$, however, scattering from neoplastic collagen fiber networks is more probable than scattering from normal collagen fiber networks. Fig. 7, *B* and *C*, further illustrates that there are no significant differences in small-angle (0–20°) scattering probabilities for normal and neoplastic networks, but high-angle (140–180°) scattering probabilities are greater for neoplastic networks.

Calculation of scattering cross sections

The scattering cross sections were calculated for all the collagen fiber networks simulated. Fig. 8 shows the averages of

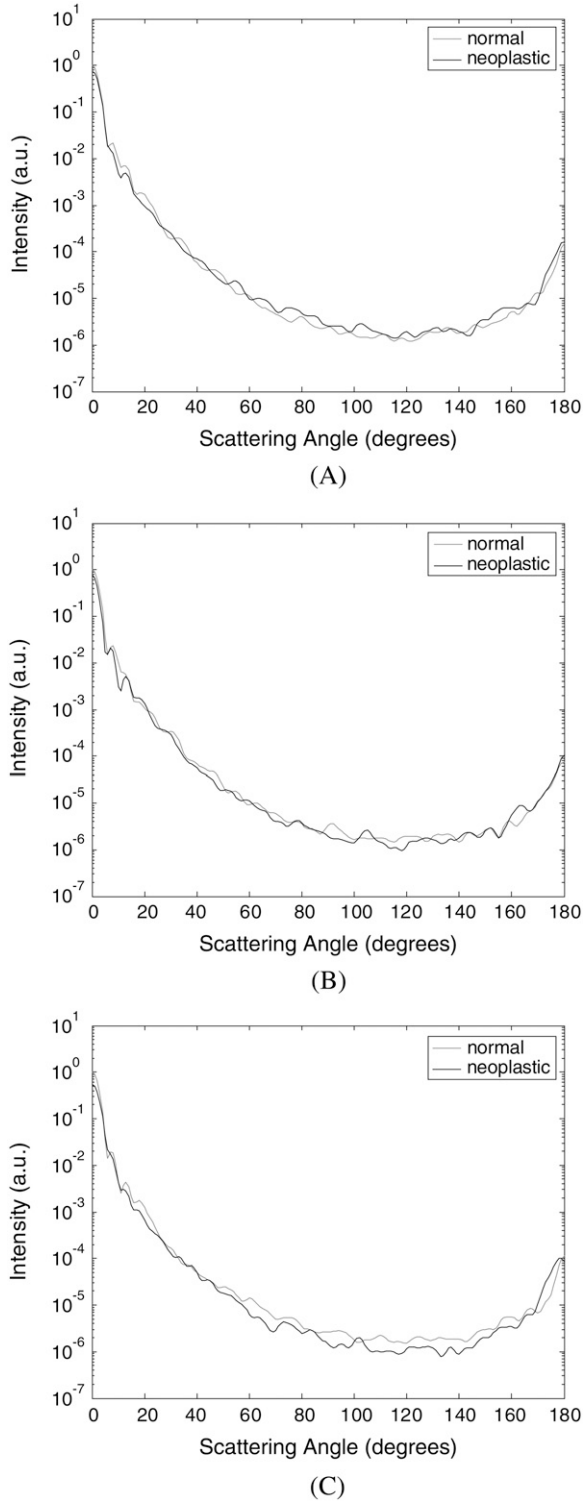

FIGURE 4 Scattering patterns averaged over four collagen fiber networks corresponding to each biopsy. The results are shown separately for (*A*) patient 1, (*B*) patient 2, and (*C*) patient 3.

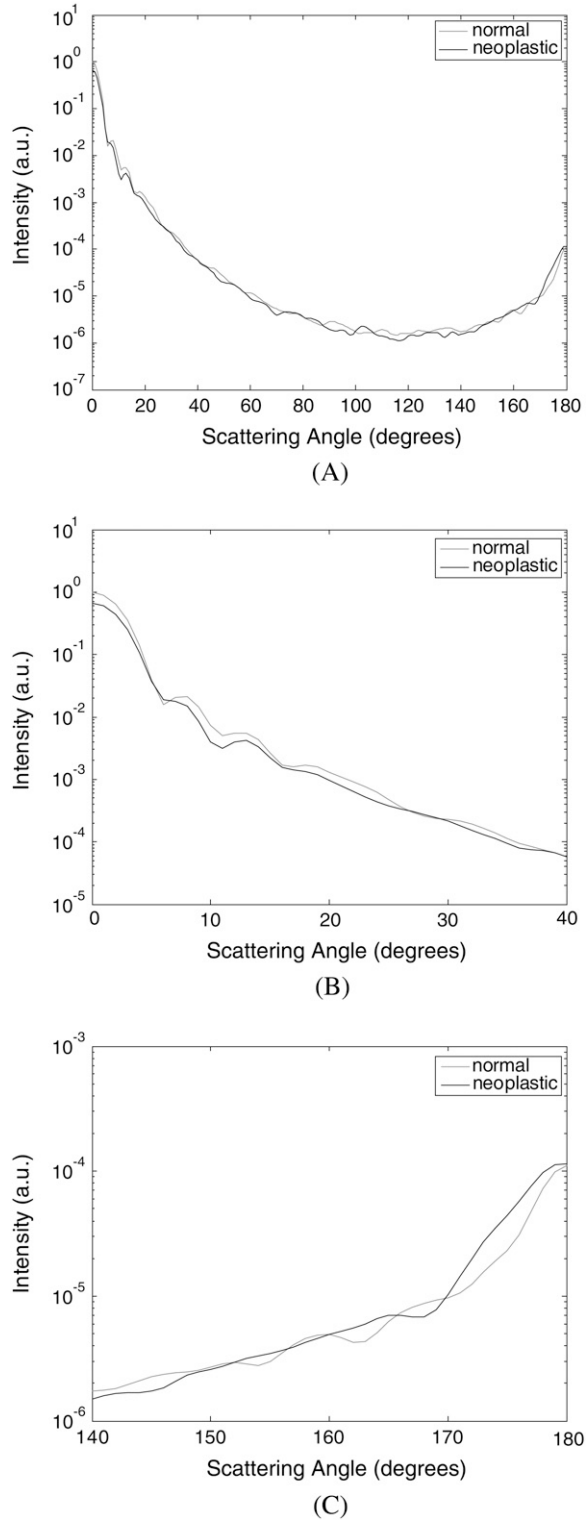

FIGURE 5 Averaged scattering patterns for normal and neoplastic collagen fiber networks over angular ranges (*A*) 0–180°, (*B*) 0–40°, and (*C*) 140–180°.

the scattering cross-section values for normal and neoplastic networks corresponding to each biopsy. The scattering cross-section values are greater for the normal networks. For the first patient, the average cross section for the neoplastic networks

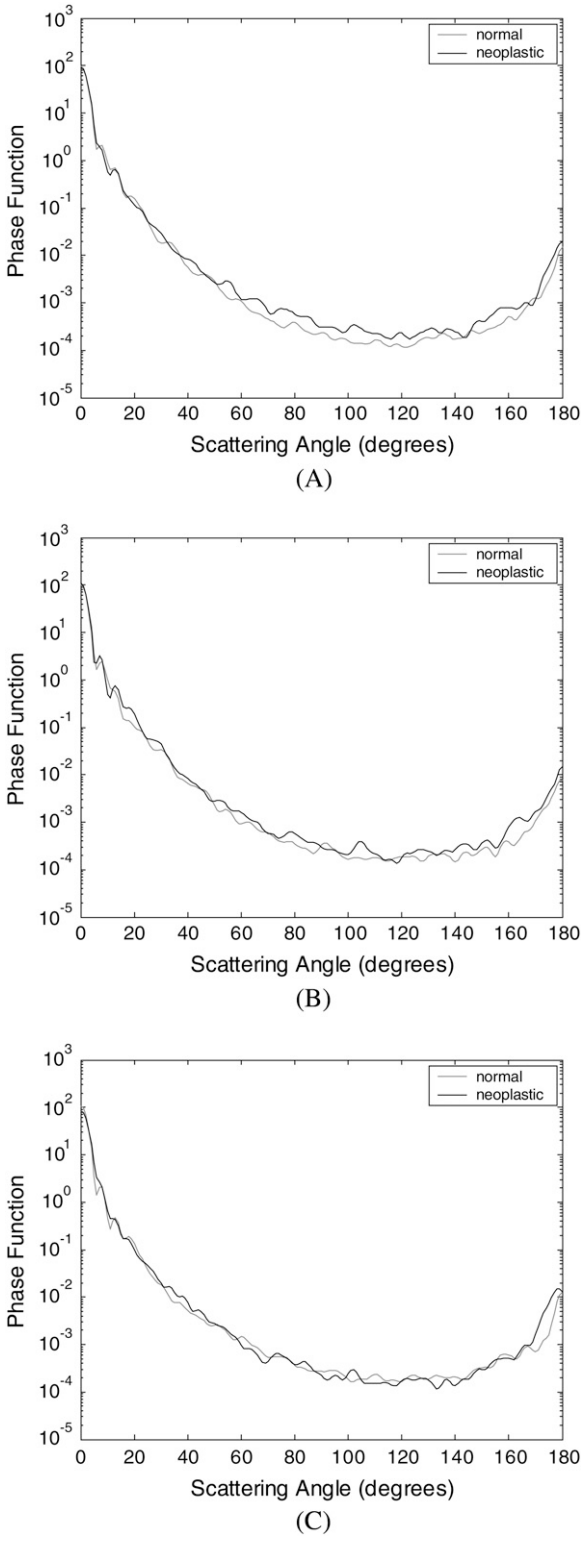

FIGURE 6 Phase functions averaged over four collagen fiber networks corresponding to each biopsy. The results are shown separately for (*A*) patient 1, (*B*) patient 2, and (*C*) patient 3.

is ~20% smaller than the average cross section for the normal networks. For the second and third patients, the difference is ~30%. The error bars shown in Fig. 8 represent the 95% Student's *t* confidence intervals computed under the assumption that the cross-section values come from a normal distribution. The results indicate that the average scattering cross-section values of the normal and neoplastic networks are different with 95% confidence for the second and third patients. The confidence intervals for the first patient overlap. A *t*-test performed on the cross-section values for the first patient resulted in a *p*-value of 0.07, suggesting that the averages are different with 90% confidence.

Trends in high-angle scattering properties

Optical imaging techniques such as RCM, OCT, and OCM are sensitive to high-angle scattering properties of tissue constituents. Assuming a numerical aperture of ~0.8 for the collection optics, scattering over the angular range 140–180° is of particular interest. To assess any differences in scattered light collected with these imaging techniques, the scattering patterns computed for each collagen fiber network can be integrated over this angular range. Fig. 9 illustrates the high-angle scattering properties of the collagen networks simulated. Fig. 9 *A* shows the scattering intensities integrated over 140–180°. To highlight the differences in relative high-angle scattering probabilities of normal and neoplastic collagen fiber networks, Fig. 9 *B* shows the phase functions integrated over the same angular range. The error bars shown in Fig. 9, *A* and *B*, represent the 95% Student's *t* confidence intervals computed under the assumption that the data values come from a normal distribution. Integrated scattering intensities tend to be higher for the neoplastic networks, but the confidence intervals shown in Fig. 9 *A* indicate that there can be extensive variability among networks from the same biopsy. A *t*-test performed on the integrated scattering intensities resulted in *p*-values that are >0.25 for all three patients. Therefore, the differences in integrated scattering intensities for the normal and neoplastic collagen fiber networks are not statistically significant. The differences in integrated phase functions shown in Fig. 9 *B*, however, appear to be more significant. For the first patient, the average high-angle scattering probability for the neoplastic networks is ~60% higher compared to the normal networks. For the second patient, the difference is ~65%, and for the third patient, the difference is ~50%. The confidence intervals shown in Fig. 9 *B* indicate that the average high-angle scattering probabilities for normal and neoplastic networks are different with 95% confidence for the first and third patients. The confidence intervals for the second patient overlap, but a *t*-test performed on the high-angle scattering probability values resulted in a *p*-value of 0.03, suggesting that the averages for this patient are also different with 95% confidence. Increased high-angle scattering probabilities for the neoplastic networks are consistent with the trends observed in Fig. 7.

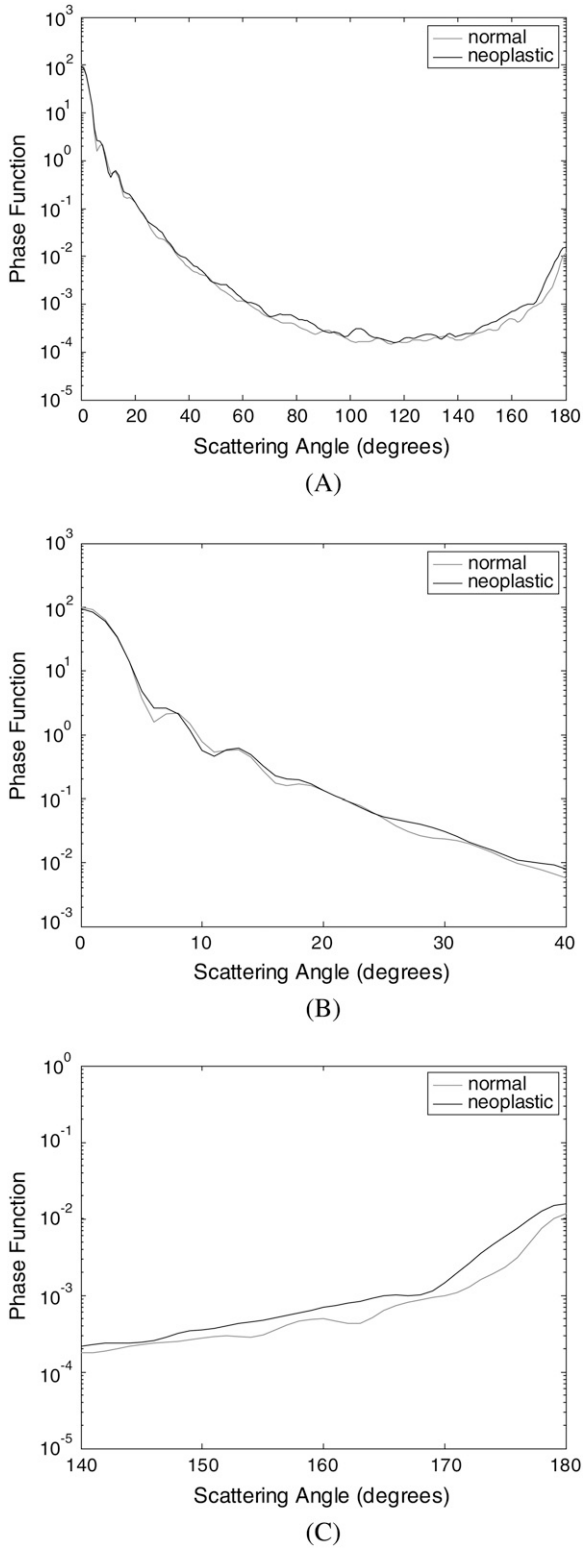

FIGURE 7 Averaged phase functions for normal and neoplastic collagen fiber networks over angular ranges (*A*) 0–180°, (*B*) 0–40°, and (*C*) 140–180°.

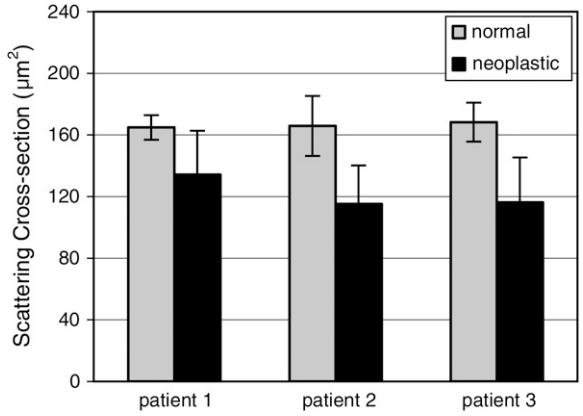

FIGURE 8 Scattering cross sections for normal and neoplastic collagen fiber networks. The results for the three patients are shown separately. The error bars represent the 95% confidence intervals.

Influence of volume fraction and spatial organization of collagen fibers on the scattering properties of collagen fiber networks

The scatter plots in Figs. 10 and 11 provide an explicit connection between the volume fraction and spatial organization

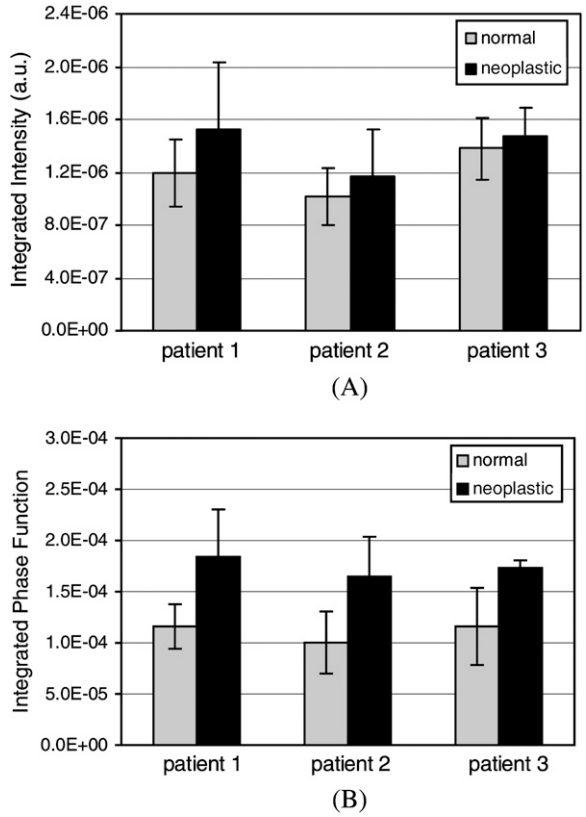

FIGURE 9 High-angle scattering properties of normal and neoplastic collagen networks. (*A*) Scattering intensities and (*B*) phase functions, both integrated over the angular range 140–180°. The results for the three patients are shown separately. The error bars represent the 95% confidence intervals.

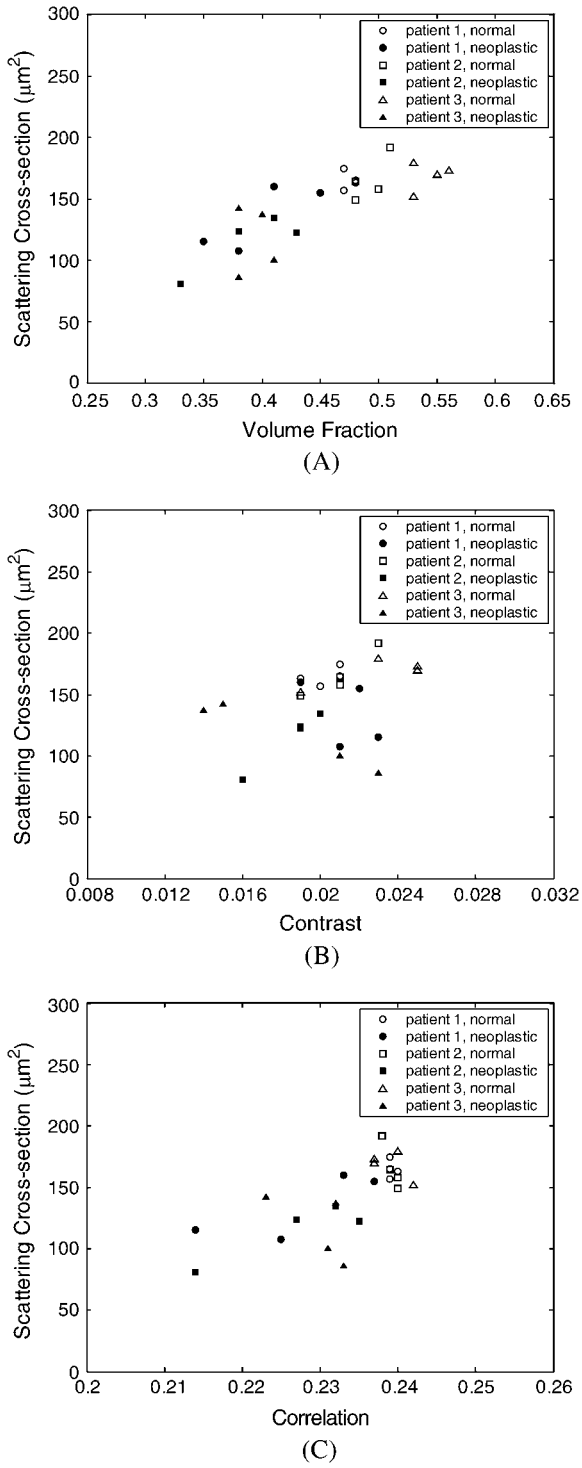

FIGURE 10 Dependence of scattering cross section on (*A*) volume fraction, (*B*) contrast, and (*C*) correlation.

of collagen fibers, and the computed scattering properties of the collagen fiber networks. Fig. 10 illustrates the dependence of scattering cross section on volume fraction, contrast, and correlation. Scattering cross section is highly correlated to volume fraction of collagen fibers and increases with increasing volume fraction. There is also good separation between normal and neoplastic cases. There is no particular trend for the contrast values, but scattering cross section is also highly dependent on correlation, with good separation between normal and neoplastic cases.

Fig. 11 focuses on the high-angle scattering properties of the networks and shows the dependence of scattering intensity and phase function, both integrated over 140–180°, on the same structural parameters as in Fig. 10. Results shown in Fig. 11 indicate that integrated scattering intensity has no apparent dependence on volume fraction, contrast, or correlation. Integrated phase function, on the other hand, is highly correlated to volume fraction and tends to decrease as volume fraction increases. Note that this trend is opposite to that observed for the cross section, which increases with increasing volume fraction. Integrated phase function also tends to assume lower values as correlation increases.

DISCUSSION

Trends in structural properties of normal and neoplastic collagen fiber networks

Most studies analyzing morphological, structural, and architectural changes that accompany development of epithelial precancer have focused on the epithelium. Dysplastic changes in epithelial cells, including increased nuclear size and irregular chromatin clumping, have been well-documented, and extraction of such nuclear features from optical signals obtained using scattering-based imaging and spectroscopic techniques has been of great interest (17–22,37,38,41). Atypical features in epithelial cells constitute one of the major pathological trademarks of preinvasive cancer (3), and extraction of these features from optical signals provides a basis to assess the diagnostic performance of optical technologies by directly comparing the results to routine histologic findings.

Cancer progression is also accompanied by mechanisms that lead to remodeling of the stroma and, hence, structural variations in the collagen matrix (46,47,57). The autofluorescence images shown in Fig. 1 illustrate typical differences between normal and neoplastic stroma. Collagen matrix of the normal stroma is denser, whereas the matrix of the neoplastic stroma appears loose and degraded. Collagen fibers in the neoplastic stroma have a more disorganized appearance in the sense that they are shorter and more detached from each other, and they also have an irregular aggregation tendency. These characteristics are consistent with autofluorescence patterns observed in stroma of normal and neoplastic epithelial tissue (48,49).

The parameters given in Table 1 quantify structural and organizational tendencies of collagen fibers. The results confirm that volume fraction of collagen fibers in the stroma tends to decrease with cancer progression. Statistical features computed provide some insight into organization of fibers in

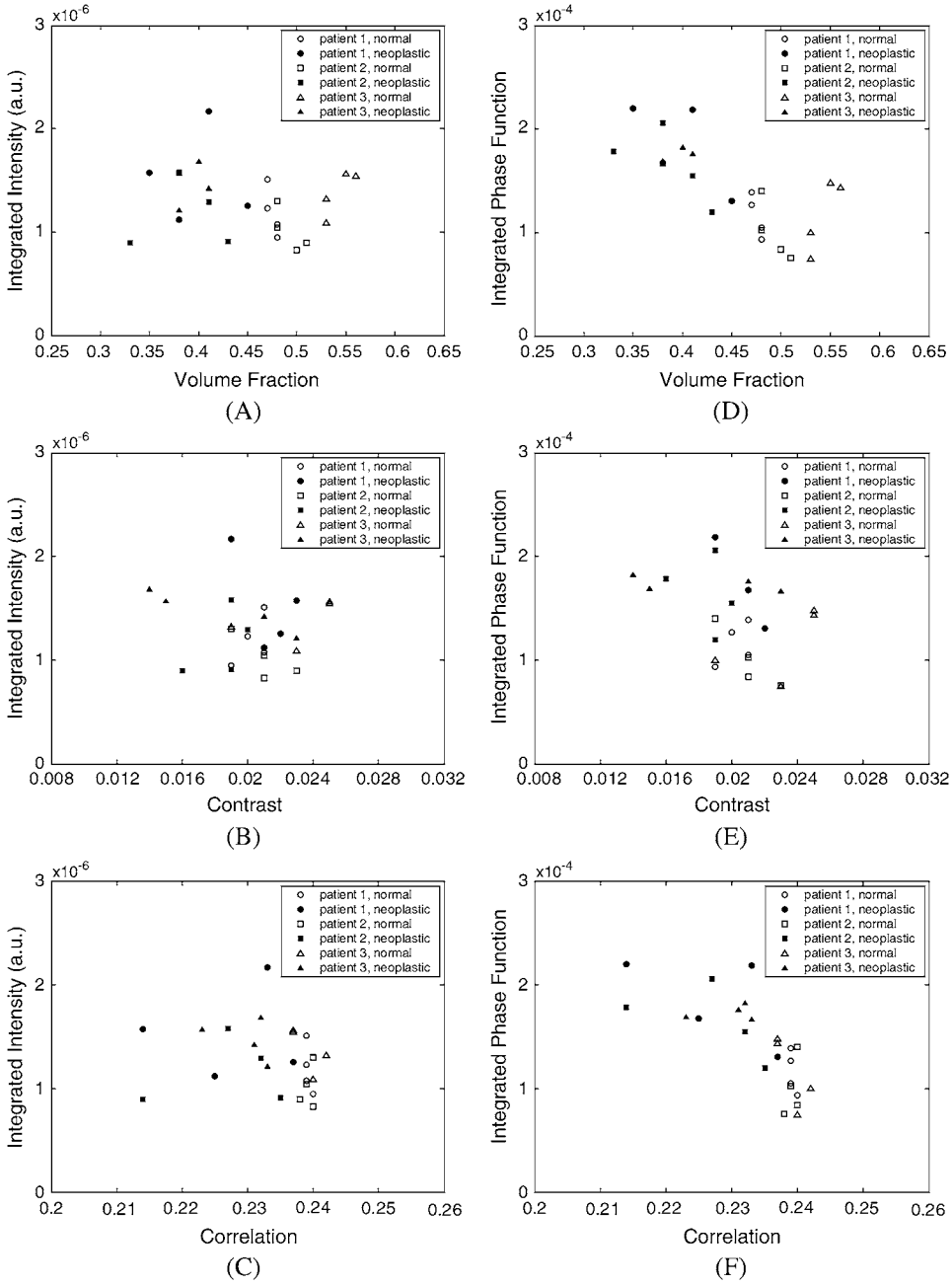

FIGURE 11 Dependence of scattering intensity and phase function, respectively, both integrated over 140–180°, on (*A* and *D*) volume fraction, (*B* and *E*) contrast, and (*C* and *F*) correlation.

the collagen matrix. Although the presence of shorter and more disconnected fibers in the case of neoplastic stroma would intuitively suggest increased contrast, the results shown in Table 1 and Fig. 3, *A* and *C*, imply no such trend. This can be explained by the fact that although degradation of fibers may result in a greater number of fiber segments, this does not automatically lead to more frequent intensity transitions in the images. Extra space created between fiber segments can be regarded as additional constant intensity regions that negate the effect of intensity transitions brought about by fiber breakdown. Therefore, contrast may not have the potential to reveal structural differences in the stroma. Correlation values for normal and neoplastic networks, on the other hand, are statistically different. Correlation is consistently lower for the neoplastic collagen fiber networks. It is important to note that correlation values increase with increasing volume fraction, as evidenced in Fig. 3 *B*. This, however, does not imply that decreased correlation for neoplastic networks is necessarily a result of decreased volume fraction. The definition of correlation in Eq. 4 ensures that decreased volume fraction does not always lead to a decrease in correlation, and it is entirely possible for a three-dimensional structure to have a smaller volume fraction and yet a higher correlation value. Thus, interdependence of volume fraction and correlation is a characteristic of the collagen fiber networks created, and decrease in both of these

parameters simultaneously suggests that loss of collagen with cancer progression is accompanied by increased disorder. Similar arguments can be made for the two-dimensional structural and organizational parameters presented in Table 2 and in Fig. 3, *D–F*.

Light-scattering properties of normal and neoplastic collagen fiber networks

FDTD simulation results indicate that neoplastic changes in stromal collagen matrix lead to decreased small-angle scattering. This is especially evident from the scattering patterns shown in Fig. 5. The scattering cross sections in Fig. 8 characterize the overall strength of scattering from the collagen fiber networks created. For highly forward scattering structures, scattering cross sections are dominated by the small-angle scattering intensities. Therefore, the fact that neoplastic networks have smaller cross sections is a manifestation of decreased small-angle scattering intensities. The phase functions in Fig. 7 show that for angles $>20°$, scattering is more probable in the case of neoplastic networks. Integrated phase functions in Fig. 9 further verify this observation for the angular range 140–180°.

Scatter plots in Fig. 10 demonstrate that volume fraction and correlation strongly influence scattering cross section. Decreased scattering cross section with progression of neoplasia is a direct consequence of decreased volume fraction and correlation. Fig. 11, on the other hand, illustrates that decrease in these parameters has the opposite effect on high-angle scattering probabilities. Integrated phase functions, however, appear to have a stronger dependence on volume fraction than on correlation. Note that since volume fraction and correlation are interdependent, it is not possible to deconvolve the effects of these two structural parameters and make independent conclusions about their exclusive influence on scattering properties of collagen networks.

Although the FDTD simulations presented provide important insight into the micro-optical properties of fibrous collagen networks, it is important to discuss some of the assumptions made in our analysis. First, we used fluorescence confocal images to provide input for FDTD scattering analysis. This leads to the question of whether all of the collagen that contributes to scattering is fluorescent and detectable through fluorescence imaging. Comparison of autofluorescence and reflectance images (not shown) obtained with a dual-mode confocal microscope reveals that stromal architecture is comparable in both, providing evidence that collagen contributing to scattering is also fluorescent.

The lateral and axial resolutions of the fluorescence confocal microscope used in our study were adequate to resolve the diameter of collagen fibers. Therefore, structural and organizational differences between normal and neoplastic collagen networks could easily be assessed. An important question is whether there are changes in the ultrastructure of collagen fibrils as neoplasia develops, and whether such changes, if there are any, contribute to the alteration of the scattering properties of neoplastic stroma. Our study is not targeted toward analyzing the effects of ultrastructural properties of collagen fibrils on the resulting scattering profile. We have rather focused on more global structural and organizational properties at the level of collagen fiber networks.

Also, note that our analysis was based on collagen fiber networks that had a size of 8 μm $\times$ 8 μm $\times$ 8 μm. Since the major aim of our study was to analyze the relative scattering properties of normal and neoplastic collagen fiber networks, we kept the overall size of the scattering structure fixed and we rather focused on the differences resulting from morphological, structural, and organizational changes that accompany neoplastic progression. We have, however, carried out extra FDTD simulations to assess the effect of network size on scattering predictions. Simulations have been performed with collagen networks of sizes that ranged between 4 and 12 μm. The results (not shown) indicate that the relative differences between the scattering properties of normal and neoplastic networks do not depend strongly on size. Networks as small as 4 μm $\times$ 4 μm $\times$ 4 μm and networks as large as 12 μm $\times$ 12 μm $\times$ 12 μm are characterized by trends similar to those presented for 8 μm $\times$ 8 μm $\times$ 8 μm collagen networks; forward scattering is higher for normal networks, whereas high-angle scattering is more probable in the case of neoplastic networks. It is of course expected that the overall strength of scattering will increase with increasing size of the scattering structure. The simulation results show that the scattering cross section increases with increasing size of the collagen networks given that volume fractions and correlation values are comparable. It should be emphasized that there is a significant advantage of analyzing networks with sizes close to 8 μm $\times$ 8 μm $\times$ 8 μm. We know that epithelial cell nuclei have sizes in the range 6–9 μm (34,35). By keeping the size of the collagen networks simulated close to the size range of the epithelial cell nuclei, we can make a direct comparison between scattering properties of these different tissue constituents. Scattering cross sections computed for epithelial cell nuclei at the same wavelength are on the order of 20 μm^2 for normal cells and 80 μm^2 for dysplastic cells (35). Comparison of the scattering cross sections in Fig. 8 to these values reveals the highly scattering nature of collagen fiber networks. Especially for normal tissue, the scattering strength of collagen networks is about eight times the scattering strength of epithelial cell nuclei. This result is consistent with significant differences observed in scattering coefficients reported for epithelial and stromal layers of normal tissue (36,39). It is also important to note that the measured scattering coefficients for stroma range from 200 to 300 cm^{-1} (36–39), corresponding to a mean scattering pathlength of $\sim$30–50 μm. This is well above the collagen network size range we consider, indicating that we are working in the single scattering regime and multiple scattering effects are not expected to play a role in the results presented.

As invasive cancer develops, tumor cells can invade the stroma and the presence of these cells amid the collagen fiber network can significantly influence the scattering properties of the stromal layer. In such cases, it is necessary to consider scattering that arises from cells in addition to scattering that arises from collagen fibers. It is possible, however, to identify cells in fluorescence confocal images of tissue biopsies, and visual examination of the images used in our study indicates that no tumor cells were present in the stromal image sections processed. Therefore, the analysis presented in this article is focused on neoplastic changes in scattering properties that entirely result from structural and morphological changes in collagen fibers.

Recent evidence suggests that neoplastic progression leads to decreased scattering in the stroma. Studies by Georgakoudi et al. (37) and Müller et al (38) describe extraction of tissue optical properties from spectroscopic measurements, and the results presented indicate that stromal scattering coefficient decreases with development of neoplasia. Since collagen fiber networks are extremely heterogeneous scattering structures, conversion of the scattering cross sections computed using the FDTD method to bulk scattering coefficients requires profound theoretical considerations. It is obvious, however, that smaller FDTD cross sections characterizing neoplastic fiber networks are consistent with the trends reported in these previous experimental studies.

Decrease in overall scattering from collagen fiber networks brought about by cancer progression and the corresponding increase in high-angle scattering probability have important implications for diagnostic optical imaging and spectroscopy. Differences in scattering properties of normal and neoplastic collagen matrix need to be taken into account when developing models of light propagation through the stromal layer, or when analyzing optical signals acquired from epithelial tissues.

This work was supported by the National Cancer Institute (grants PO1 CA82710 and RO1 CA095604).

REFERENCES

1. Jemal, A., R. Siegel, E. Ward, T. Murray, J. Xu, C. Smigal, and M. J. Thun. 2006. Cancer statistics, 2006. *CA Cancer J. Clin.* 56:106–130.
2. American Cancer Society. 2006. Cancer Facts and Figures 2006. American Cancer Society, Atlanta.
3. Koss, L. G. 1992. Diagnostic Cytology and Its Histopathologic Bases. Lippincott, Philadelphia.
4. Mueller, M. M., and N. E. Fusenig. 2002. Tumor-stroma interactions directing phenotype and progression of epithelial skin tumor cells. *Differentiation.* 70:486–497.
5. Pupa, S. M., S. Menard, S. Forti, and E. Tagliabue. 2002. New insights into the role of extracellular matrix during tumor onset and progression. *J. Cell. Physiol.* 192:259–267.
6. Bhowmick, N. A., and H. L. Moses. 2005. Tumor-stroma interactions. *Curr. Opin. Genet. Dev.* 15:97–101.
7. Zigrino, P., S. Löffek, and C. Mauch. 2005. Tumor-stroma interactions: their role in the control of tumor cell invasion. *Biochimie.* 87:321–328.
8. Hong, W. K., and M. B. Sporn. 1997. Recent advances in chemoprevention of cancer. *Science.* 278:1073–1077.
9. Ingber, D. E. 2002. Cancer as a disease of epithelial-mesenchymal interactions and extracellular matrix regulation. *Differentiation.* 70:547–560.
10. Bogenrieder, T., and M. Herlyn. 2003. Axis of evil: molecular mechanisms of cancer metastasis. *Oncogene.* 22:6524–6536.
11. Wagnieres, G. A., W. M. Star, and B. C. Wilson. 1998. In vivo fluorescence spectroscopy and imaging for oncological applications. *Photochem. Photobiol.* 68:603–632.
12. Lam, S., T. Kennedy, M. Unger, Y. E. Miller, D. Gelmont, V. Rusch, B. Gipe, D. Howard, J. C. LeRiche, A. Coldman, and A. F. Gazdar. 1998. Localization of bronchial intraepithelial neoplastic lesions by fluorescence bronchoscopy. *Chest.* 113:696–702.
13. Bigio, I. J., S. G. Bown, G. Briggs, C. Kelley, S. Lakhani, D. Pickard, P. M. Ripley, I. G. Rose, and C. Saunders. 2000. Diagnosis of breast cancer using elastic-scattering spectroscopy: preliminary clinical results. *J. Biomed. Opt.* 5:221–228.
14. Fujimoto, J. G., C. Pitris, S. A. Boppart, and M. E. Brezinski. 2000. Optical coherence tomography: an emerging technology for biomedical imaging and optical biopsy. *Neoplasia.* 2:9–25.
15. Langley, R. G. B., M. Rajadhyaksha, P. J. Dwyer, A. J. Sober, T. J. Flotte, and R. R. Anderson. 2001. Confocal scanning laser microscopy of benign and malignant melanocytic skin lesions in vivo. *J. Am. Acad. Dermatol.* 45:365–376.
16. Shah, N., A. Cerussi, C. Eker, J. Espinoza, J. Butler, J. Fishkin, R. Hornung, and B. Tromberg. 2001. Noninvasive functional optical spectroscopy of human breast tissue. *Proc. Natl. Acad. Sci. USA.* 98:4420–4425.
17. Sokolov, K., M. Follen, and R. Richards-Kortum. 2002. Optical spectroscopy for detection of neoplasia. *Curr. Opin. Chem. Biol.* 6:651–658.
18. Sokolov, K., K. Sung, T. Collier, A. Clark, D. Arifler, A. Lacy, M. Descour, and R. Richards-Kortum. 2002. Endoscopic microscopy. *Dis. Markers.* 18:269–291.
19. Badizadegan, K., V. Backman, C. W. Boone, C. P. Crum, R. R. Dasari, I. Georgakoudi, K. Keefe, K. Munger, S. M. Shapshay, E. E. Sheets, and M. S. Feld. 2004. Spectroscopic diagnosis and imaging of invisible pre-cancer. *Faraday Discuss.* 126:265–279.
20. Mourant, J. R., J. P. Freyer, A. H. Hielscher, A. A. Eick, D. Shen, and T. M. Johnson. 1998. Mechanisms of light scattering from biological cells relevant to noninvasive optical-tissue diagnostics. *Appl. Opt.* 37:3586–3593.
21. Backman, V., R. Gurjar, K. Badizadegan, I. Itzkan, R. R. Dasari, L. T. Perelman, and M. S. Feld. 1999. Polarized light scattering spectroscopy for quantitative measurement of epithelial cellular structures in situ. *IEEE J. Sel. Top. Quantum Electron.* 5:1019–1026.
22. Sokolov, K., R. A. Drezek, K. Gossage, and R. R. Richards-Kortum. 1999. Reflectance spectroscopy with polarized light: is it sensitive to cellular and nuclear morphology? *Opt. Express.* 5:302–317.
23. Mishchenko, M. I., J. W. Hovenier, and L. D. Travis, editors. 2000. Light Scattering by Nonspherical Particles: Theory, Measurements, and Applications. Academic Press, San Diego.
24. Li, X., Z. Chen, A. Taflove, and V. Backman. 2004. Equiphase-sphere approximation for light scattering by stochastically inhomogeneous microparticles. *Phys. Rev. E.* 70:056610.
25. Wilson, J. D., C. E. Bigelow, D. J. Calkins, and T. H. Foster. 2005. Light scattering from intact cells reports oxidative-stress-induced mitochondrial swelling. *Biophys. J.* 88:2929–2938.
26. Wilson, J. D., and T. H. Foster. 2005. Mie theory interpretations of light scattering from intact cells. *Opt. Lett.* 30:2442–2444.
27. Dunn, A., and R. Richards-Kortum. 1996. Three-dimensional computation of light scattering from cells. *IEEE J. Sel. Top. Quantum Electron.* 2:898–905.
28. Drezek, R., A. Dunn, and R. Richards-Kortum. 1999. Light scattering from cells: finite-difference time-domain simulations and goniometric measurements. *Appl. Opt.* 38:3651–3661.
29. Boustany, N. N., R. Drezek, and N. V. Thakor. 2002. Calcium-induced alterations in mitochondrial morphology quantified in situ with optical scatter imaging. *Biophys. J.* 83:1691–1700.

30. Jiangping, H., A. Karlsson, J. Swartling, and S. Andersson-Engels. 2004. Light scattering by multiple red blood cells. *J. Opt. Soc. Am. A Opt. Image Sci. Vis.* 21:1953–1961.

31. Liu, C., C. Capjack, and W. Rozmus. 2005. 3-D simulation of light scattering from biological cells and cell differentiation. *J. Biomed. Opt.* 10:014007.

32. Collier, T., A. Lacy, R. Richards-Kortum, A. Malpica, and M. Follen. 2002. Near real-time confocal microscopy of amelanotic tissue: detection of dysplasia in ex vivo cervical tissue. *Acad. Radiol.* 9:504–512.

33. Clark, A. L., A. M. Gillenwater, T. G. Collier, R. Alizadeh-Naderi, A. K. El-Naggar, and R. R. Richards-Kortum. 2003. Confocal microscopy for real-time detection of oral cavity neoplasia. *Clin. Cancer Res.* 9: 4714–4721.

34. Drezek, R., M. Guillaud, T. Collier, I. Boiko, A. Malpica, C. MacAulay, M. Follen, and R. Richards-Kortum. 2003. Light scattering from cervical cells throughout neoplastic progression: influence of nuclear morphology, DNA content, and chromatin texture. *J. Biomed. Opt.* 8:7–16.

35. Arifler, D., M. Guillaud, A. Carraro, A. Malpica, M. Follen, and R. Richards-Kortum. 2003. Light scattering from normal and dysplastic cervical cells at different epithelial depths: finite-difference time-domain modeling with a perfectly matched layer boundary condition. *J. Biomed. Opt.* 8:484–494.

36. Qu, J., C. MacAulay, S. Lam, and B. Palcic. 1994. Optical properties of normal and carcinomatous bronchial tissue. *Appl. Opt.* 33:7397–7405.

37. Georgakoudi, I., E. E. Sheets, M. G. Müller, V. Backman, C. P. Crum, K. Badizadegan, R. R. Dasari, and M. S. Feld. 2002. Trimodal spectroscopy for the detection and characterization of cervical precancers in vivo. *Am. J. Obstet. Gynecol.* 186:374–382.

38. Müller, M. G., T. A. Valdez, I. Georgakoudi, V. Backman, C. Fuentes, S. Kabani, N. Laver, Z. Wang, C. W. Boone, R. R. Dasari, S. M. Shapshay, and M. S. Feld. 2003. Spectroscopic detection and evaluation of morphologic and biochemical changes in early human oral carcinoma. *Cancer.* 97:1681–1692.

39. Collier, T., M. Follen, A. Malpica, and R. Richards-Kortum. 2005. Sources of scattering in cervical tissue: determination of the scattering coefficient by confocal microscopy. *Appl. Opt.* 44:2072–2081.

40. Skala, M. C., G. M. Palmer, C. Zhu, Q. Liu, K. M. Vrotsos, C. L. Marshek-Stone, A. Gendron-Fitzpatrick, and N. Ramanujam. 2004. Investigation of fiber-optic probe designs for optical spectroscopic diagnosis of epithelial pre-cancers. *Lasers Surg. Med.* 34:25–38.

41. Nieman, L., A. Myakov, J. Aaron, and K. Sokolov. 2004. Optical sectioning using a fiber probe with an angled illumination-collection geometry: evaluation in engineered tissue phantoms. *Appl. Opt.* 43:1308–1319.

42. Kim, Y. L., Y. Liu, R. K. Wali, H. K. Roy, and V. Backman. 2005. Low-coherent backscattering spectroscopy for tissue characterization. *Appl. Opt.* 44:366–377.

43. Schwarz, R. A., D. Arifler, S. K. Chang, I. Pavlova, I. A. Hussain, V. Mack, B. Knight, R. Richards-Kortum, and A. M. Gillenwater. 2005. Ball lens coupled fiber-optic probe for depth-resolved spectroscopy of epithelial tissue. *Opt. Lett.* 30:1159–1161.

44. Arifler, D., R. A. Schwarz, S. K. Chang, and R. Richards-Kortum. 2005. Reflectance spectroscopy for diagnosis of epithelial precancer: model-based analysis of fiber-optic probe designs to resolve spectral information from epithelium and stroma. *Appl. Opt.* 44:4291–4305.

45. Wang, A. M. J., J. E. Bender, J. Pfefer, U. Utzinger, and R. A. Drezek. 2005. Depth-sensitive reflectance measurements using obliquely oriented fiber probes. *J. Biomed. Opt.* 10:044017.

46. Heppner, K. J., L. M. Matrisian, R. A. Jensen, and W. H. Rodgers. 1996. Expression of most matrix metalloproteinase family members in breast cancer represents a tumor-induced host response. *Am. J. Pathol.* 149:273–282.

47. Parks, W. C. 1998. Matrix Metalloproteinases. Academic Press, San Diego.

48. Pavlova, I., K. Sokolov, R. Drezek, A. Malpica, M. Follen, and R. Richards-Kortum. 2003. Microanatomical and biochemical origins of normal and precancerous cervical autofluorescence using laser-scanning fluorescence confocal microscopy. *Photochem. Photobiol.* 77: 550–555.

49. Wilder-Smith, P., K. Osann, N. Hanna, N. El Abbadi, M. Brenner, D. Messadi, and T. Krasieva. 2004. In vivo multiphoton fluorescence imaging: a novel approach to oral malignancy. *Lasers Surg. Med.* 35: 96–103.

50. Freund, D. E., R. L. McCally, and R. A. Farrell. 1986. Effects of fibril orientations on light scattering in the cornea. *J. Opt. Soc. Am. A Opt. Image Sci. Vis.* 3:1970–1982.

51. Saidi, I. S., S. L. Jacques, and F. K. Tittel. 1995. Mie and Rayleigh modeling of visible-light scattering in neonatal skin. *Appl. Opt.* 34: 7410–7418.

52. Ross, M. H., L. J. Romrell, and G. I. Kaye. 1995. Histology: A Text and Atlas. Lippincott, Baltimore.

53. Ushiki, T. 2002. Collagen fibers, reticular fibers and elastic fibers: a comprehensive understanding from a morphological viewpoint. *Arch. Histol. Cytol.* 65:109–126.

54. Eyden, B., and M. Tzaphlidou. 2001. Structural variations of collagen in normal and pathological tissues: role of electron microscopy. *Micron.* 32:287–300.

55. Wu, J., B. Rajwa, D. L. Filmer, C. M. Hoffmann, B. Yuan, C. Chiang, J. Sturgis, and J. P. Robinson. 2003. Automated quantification and reconstruction of collagen matrix from 3D confocal datasets. *J. Microsc.* 210:158–165.

56. Richards-Kortum, R., and E. Sevick-Muraca. 1996. Quantitative optical spectroscopy for tissue diagnosis. *Annu. Rev. Phys. Chem.* 47: 555–606.

57. Friedl, P. 2004. Dynamic imaging of cellular interactions with extracellular matrix. *Histochem. Cell Biol.* 122:183–190.

58. Zipfel, W. R., R. M. Williams, R. Christie, A. Y. Nikitin, B. T. Hyman, and W. W. Webb. 2003. Live tissue intrinsic emission microscopy using multiphoton-excited native fluorescence and second harmonic generation. *Proc. Natl. Acad. Sci. USA.* 100:7075–7080.

59. Zoumi, A., X. Lu, G. S. Kassab, and B. Tromberg. 2004. Imaging coronary artery microstructure using second-harmonic and two-photon fluorescence microscopy. *Biophys. J.* 87:2778–2786.

60. Taflove, A. 1995. Computational Electrodynamics: The Finite-Difference Time-Domain Method. Artech House, Norwood, MA.

61. Taflove, A., editor. 1998. Advances in Computational Electrodynamics: The Finite-Difference Time-Domain Method. Artech House, Norwood, MA.

62. Bohren, F., and D. R. Huffman. 1998. Absorption and Scattering of Light by Small Particles. Wiley, New York.

63. Sokolov, K., J. Galvan, A. Myakov, A. Lacy, R. Lotan, and R. Richards-Kortum. 2002. Realistic three-dimensional epithelial tissue phantoms for biomedical optics. *J. Biomed. Opt.* 7:148–156.

64. Duda, R. O., P. E. Hart, and D. G. Stork. 2001. Pattern Classification. Wiley, New York.

65. Haralick, R. M., K. Shanmugam, and I. Dinstein. 1973. Textural features for image classification. *IEEE Trans. Sys. Man Cyber.* SMC-3: 610–621.

66. Soltanian-Zadeh, H., F. Rafiee-Rad, and S. Pourabdollah-Nejad. 2004. Comparison of multiwavelet, wavelet, Haralick, and shape features for microcalcification classification in mammograms. *Pattern Recogn.* 37: 1973–1986.

67. Maurice, D. M. 1957. The structure and transparency of the cornea. *J. Physiol.* 136:263–286.

68. Schmitt, J. M., and G. Kumar. 1996. Turbulent nature of refractive-index variations in biological tissue. *Opt. Lett.* 21:1310–1312.

69. Leonard, D. W., and K. M. Meek. 1997. Refractive indices of the collagen fibrils and extrafibrillar material of the corneal stroma. *Biophys. J.* 72:1382–1387.

70. Wang, X., T. E. Milner, M. C. Chang, and J. S. Nelson. 1996. Group refractive index measurement of dry and hydrated type I collagen films using optical low-coherence reflectometry. *J. Biomed. Opt.* 1:212–216.

71. Hirshburg, J., B. Choi, J. S. Nelson, and A. T. Yeh. 2006. Collagen solubility correlates with skin optical clearing. *J. Biomed. Opt.* 11:040501.